Cellulose (2025) 32:3335–3354
https://doi.org/10.1007/s10570-025-06471-5

ORIGINAL RESEARCH

Lightweight and sustainable recycled cellulose based hybrid aerogels with enhanced electromagnetic interference shielding

Bircan Haspulat Taymaz · Volkan Eskizeybek

Received: 4 October 2024 / Accepted: 2 March 2025 / Published online: 15 March 2025

Abstract Developing lightweight, sustainable, high porosity, and high-performance electromagnetic interference (EMI) shielding apparatus is essential to diminish electromagnetic contamination for protecting human health and electronic devices. Herein, 1D carbon nanotubes (CNTs) and 2D graphene nanoplatelets (GNPs) functionalized recycled cellulose aerogel (RCA) were fabricated via a facile method by freeze, solvent exchange, and ambient drying. The effect of nanofiller type and quantity on the structural, morphological, electrical, thermal and EMI shielding performance of the RC-based aerogel were investigated. The as-prepared hybrid aerogel displays the maximum 40.2 dB electromagnetic interference shielding efficiency (SE) at 8.92 dB GHz with absorption dominant characteristic. CNTs:GNPs nanofillers in recycled cellulose matrix provoked conductivity mismatching and increased interfacial polarization loss. At a density of 0.087 gcm^{-3}, CNTs:GNPs; 7:7%wt. doped RCA exhibits a highly specific SE (SSE) value of 461.95 $dBcm^3g^{-1}$ and an absolute SE (SSE/t) value of 2309.29 $dBcm^2g^{-1}$. These results show that the CNTs:GNPs; 7:7%wt. doped RCA can meet practical applications' lightweight and high-efficiency EMI shielding requirements.

Keywords Recycle cellulose · Aerogel · CNTs · GNPs · Sustainable materials · Ambient drying

Introduction

The extensive usage of electronic products leads to EM pollution, which can interfere with electronic devices and pose risks to human health (Ma et al. 2024; Zhang et al. 2024e). To control EM pollution, high-efficient and new-generation advanced EMI shielding materials are designed and implemented in daily life (Yang et al. 2024). A promising advancement in the development of EMI shielding is using conductive porous materials instead of traditional metal-based EMI shielding materials, which offer large spaces for multiple reflection and scattering EM waves (EMWs) with lightweight (Guo et al. 2020a).

Moreover, recent EMI shielding research is shifting toward sustainable and renewable materials due to global concern while reducing carbon emissions (Gebrekrstos et al. 2022). At the same, recycling processes provide an alternative way to diminish carbon emissions by consuming less energy and reusing

Supplementary Information The online version contains supplementary material available at https://doi.org/10.1007/s10570-025-06471-5.

B. Haspulat Taymaz (✉)
Department of Chemical Engineering, Konya Technical University, Konya, Türkiye
e-mail: bhaspulat@ktun.edu.tr

B. Haspulat Taymaz · V. Eskizeybek
Department of Materials Science and Engineering, Çanakkale Onsekiz Mart University, Çanakkale, Türkiye

materials rather than new materials obtained from natural sources. With the world moving toward sustainable and renewable materials, cellulose, obtained from wastepaper pulp, is crucial. From a sustainability perspective, wastepaper pulp, which contains an essential amount of cellulose fibers, is the most charming source of cellulose (Damnali and Eskizeybek 2019).

Recycled cellulose (RC) fiber owns considerable features like high surface area biodegradability, adjustable hydrogen bonds, and low cost (Gebrekrstos et al. 2022). The plentiful hydroxyl groups on cellulose chains can react with functional fillers during the recycling, allowing the fillers to be evenly distributed throughout the cellulose matrix (Qi et al. 2013). The addition of different types of nanofillers increased RC's features for designing and producing multifunctional EMI shielding materials and different types of sensors, offering a sustainable alternative to petroleum-based polymers (Jimenez-Saelices et al. 2017; Li et al. 2022a). RC can be easily manufactured in film or 3D aerogel form (Dai et al. 2024; Liu et al. 2024). Specifically, the use of RC-based 3D aerogel structures as EMI shielding materials have recently become a hot topic (Li et al. 2022a). The high surface area and network structure of RC-based aerogels increase multiple reflection efficiency and improve the EMI shielding performance (Song et al. 2021).

The production of cellulose aerogel is categorized into two main stages: i) preparation of cellulose gel and ii) removal of solvents from the aerogel skeleton (Liebner et al. 2008). In the first step, to construct a strong skeleton, a cellulose suspension should be obtained. N-methylmorpholine-N-oxide (Rosenaua et al. 2001), DMAc/LiCl (Potthast 2015) and NaOH/urea (Huang et al. 2022a) can be used to dissolve cellulose fiber. The NaOH/urea system dissolves the cellulose fibers by breaking the hydrogen bonding between the cellulose chains. Moreover, the urea prevents the skeleton's collapse by inhibiting cellulose's agglomeration to form aerogel with enhanced porosity (Wernersson et al. 2015; Xiong et al. 2014). In the second step, two techniques—freeze and supercritical drying—are commonly used to release cellulose aerogel solvents (Zhou et al. 2018). Unfortunately, freeze-drying is not scalable since it needs specialized equipment, takes a long time to process, and uses much energy (Tchessalov et al. 2022). Likewise, supercritical drying's harsh operational requirements, specialized tools, and many chemical processing stages restrict the commercialization of the method for cellulose aerogel production (Liu et al. 2024). Alternatively, ambient drying is the simplest, most practical, and scalable process (Hou et al. 2024). In ambient drying method as first step, cellulose hydrogel is introduced to a low surface tension solvent like ethanol to dissolve ice crystals in cellulose hydrogel (Xu et al. 2023). Moreover, the low surface tension of ethanol ensures skeletal structure by increasing hydrogen force. Then, the cellulose hydrogel is subject to a drying process under ambient conditions. Ebrahimi et al. produced the cellulose aerogel with a low density of 0.053 gcm^{-3} using naphthalene crystal as a porous-making agent under ambient drying conditions (Ebrahimi et al. 2020). Françon et al. developed an efficient and facile way to produce cellulose aerogel based on freezing, solvent exchange, and ambient drying steps. Also, the controlled addition of salts prevented the collapse of aerogel. (Françon et al. 2020). In another study, cellulose aerogel was fabricated using freeze-linking technology and dried under atmospheric conditions. To strengthen the fiber skeleton, a cross-linking network was created by the self-crosslink reaction of Schiff base and 3-aminopropyltriethoxysilane (Hu et al. 2023).

Although cellulose's insulating and nonmagnetic characteristics limit its application as a sole shielding substance, it can be utilized in combination with conducting fillers, like CNTs (Schiele et al. 2024), reduced graphene oxide (rGO) (Wang et al. 2024a) metal nanowires (Dai et al. 2024), and MXene (Zhao et al. 2024). One-dimensional CNTs exhibit outstanding mechanical features, low density, and an extensive aspect ratio and can easily adapt to macroscopic structures like 1D fiber, 2D films, 3D foams, and aerogel (Damnalı and Eskizeybek 2019). Another unique carbon structure, graphene, attracts significant attention due to its remarkable mechanical, thermal, and electric properties (Yun et al. 2024). Lightweight cellulose /CNT aerogels with porosity% were produced by Zu et al. with freeze-drying, which presented a EMI SE above 39.8 dB (Zhu et al. 2022). Li et al. designed CNT/cellulose aerogel by adjusting structure by tertiary butanol content and freeze drying, exhibiting an EMI SE of 22 dB and a specific EMI SE of 716 $dBcm^3g^{-1}$ (Li et al. 2022b). The cellulose/polyacrylamide/graphene nanosheets/silver nanowire aerogel was fabricated using direct freeze drying by

Wu et al. (Wu et al. 2023a). They profited from the synergistic effect between graphene nanosheets and silver nanowires. Hybrid aerogels exhibit an average EMI SE of 71.08 dB and 35.21 dB along the transverse and longitudinal directions (Wu et al. 2023a). Combining conductive nanofillers with cellulose aerogels construct can create immense effective interfaces and improve the EMI SE value by increases interfacial polarization (Han et al. 2021; Zong et al. 2022b). Therefore, designing lightweight, porous, and conductive EMI shielding materials with superior absorption capabilities of EMWs, constructed via facile and scalable processes, is essential for promoting sustainable and efficient shielding technologies.

Herein, lightweight and highly porous CNTs:GNPs doped RCA (CxGy) were successfully manufactured utilizing a sustainable, scalable, and facile approach involving freeze casting, solvent exchange, and ambient drying. This approach underestimated energy consumption and eliminated the need for specialized equipment. The aerogels' physical, structural, morphological, and electrical conductivity properties were thoroughly characterized. The EMI shielding performance was investigated in detail within the X-band frequency range (8.2–12.4 GHz), particularly emphasizing the shielding mechanisms. To enhance EMWs absorption, the synergistic effect of CNT and GNP nanostructures was utilized to construct a conductive network within the cellulose matrix. This network induced interfacial polarization losses by creating a conductivity mismatch between the conductive network and the cellulose matrix. Furthermore, the conductive network facilitated the absorption of incident EMWs within the matrix, converting electromagnetic energy into thermal energy. This study confirms the development of lightweight, absorption-dominant EMI shielding materials using carbon-based conductive nanofillers through sustainable and scalable fabrication methods.

Experimental

Obtaining of RC

The office wastepaper (OWP) which used as cellulose source cut into small pieces using a paper shredder (Omega). The shredded OWP washed with distilled water, filtered and dried at 80 °C for 24 h (Yue et al. 2018). The schematic representation of the obtaining of RC was given in Fig. 1 inset. To break the hydrogen bonds between different cellulose chains and remove hemicellulose (Akhlamadi and Goharshadi 2021), OWP and 500 ml of 5% NaOH were transferred to a bar blender and vigorously disintegrated for 5 min (OAK:NaOH; 1:20 (wt/v)). The obtained mixture was transferred to a beaker and stirred at 80 °C for 2 h at 500 rpm (Srasri et al. 2018). After the light yellow mixture reached room temperature, 2% (wt%) $NaClO_3$ 1/5 (v/v; according to the previous step) was added to whiten the color (Ghazitabar et al. 2020). Then, the pH of the mixture was adjusted to 4 with 1 M HNO_3 and stirred at 80 °C for 2 h (Akhlamadi and Goharshadi 2021). The mixture was cooled to room temperature, filtered, washed with pure water until neutralized and dried at 80 °C for 24 h to obtain RC.

Production of CxGy aerogels

In order to obtain dispersions of nanofillers and solvents, CNTs (Nanografi, Türkiye) and GNPs (Nanografi, Türkiye) were dispersed in 300 ml of a solution containing NaOH (Merck), urea (Merck), and water (in a ratio of 7:12:81, wt:wt:wt). The specified amount of CNTs and GNPs (as outlined in Table 1) were added to the solution. In the sample coding, 'C' and 'G' denote CNT and GNP, respectively, which are added to the production medium, while 'x' and 'y' indicate their corresponding weight percentages. The colloids were sonicated sequentially via a tip sonicator (Bandelin UW3400) in an ice bath for 15 min to prevent any structural damage to the carbon nanostructures. The sonication was carried out at 20% of the maximum amplitude (Damnalı and Eskizeybek 2019). The mixture was poured out into a high-speed bar blender (Vortex Pro, Kitchen), and 0.99 g of RC was added. The mixture was mixed for 5 min at 24,000 rpm and immediately transferred to the molding process. In this step, 30 ml of the mixture was poured into the molds. The molds were then kept in a deep freezer at −18 °C for 24 h. The frozen mixture was carefully removed from the mold and placed in ethanol solution for 24 h in ethanol. The hydrogel was dried in an oven at 40 °C for 24 h. Additionally, the neat RC was prepared as the control group sample using the same procedure, but without the nanofiller.

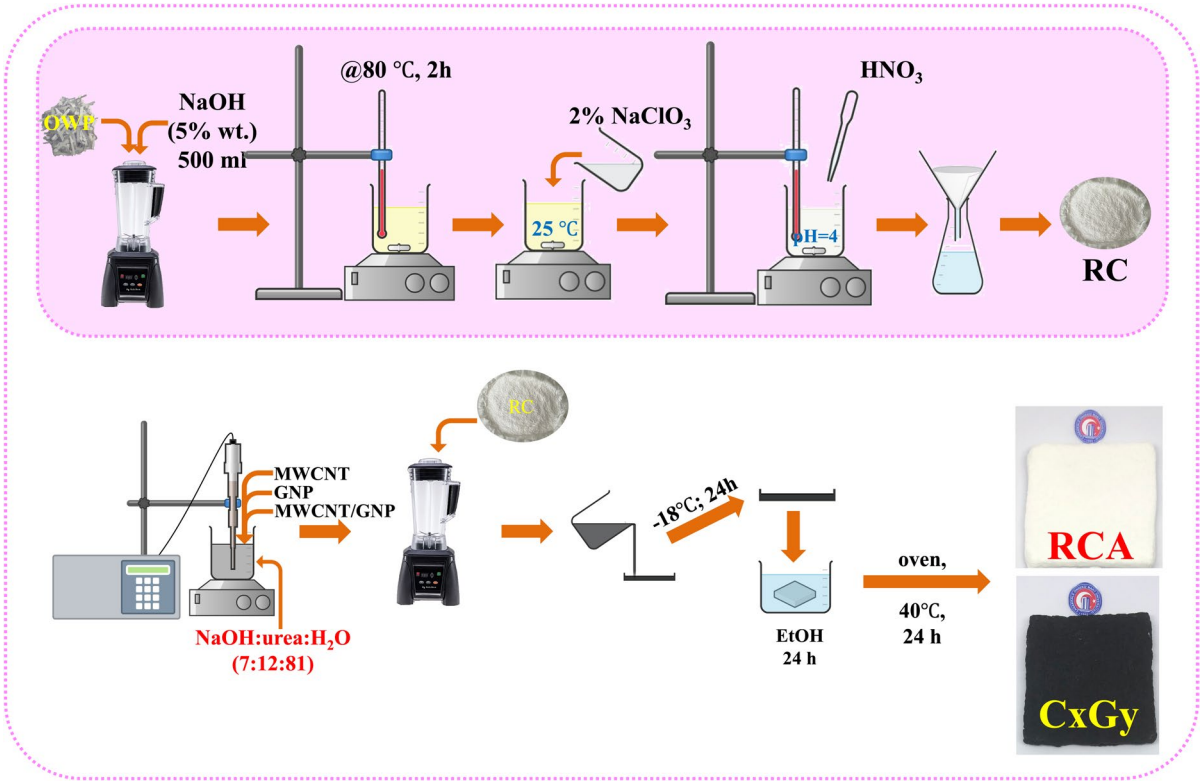

Fig. 1 The schematic representation of production of RC, RCA and CxGy

Table 1 Nanofiller ratios and sample codes of produced CxGy samples

RC amount (g)	MWCNT% (wt.)	GNP% (wt.)	Sample code
0.99	3	0	C3G0
0.99	3	3	C3G3
0.99	3	7	C3G7
0.99	3	10	C3G10
0.99	7	0	C7G0
0.99	7	3	C7G3
0.99	7	7	C7G7
0.99	7	10	C7G10
0.99	10	0	C10G0
0.99	10	3	C10G3
0.99	10	7	C10G7
0.99	10	10	C10G10
0.99	0	3	C0G3
0.99	0	7	C0G7
0.99	0	10	C0G10
0.99	0	0	RCA

Characterization

The apparent density of the produced aerogels was examined by measuring their mass and volume. The mass of the aerogels was weighted by an analytical balance (Mettler Toledo) and the volume was calculated by measuring their diameters and heights using a digital caliper (Fujisan) at three different positions. In calculation of porosity of the aerogels, *P*, only cellulose, CNTs and GNPs are based. The porosity, P, was computed according to Eq. (1) (Prasad et al. 2024):

$$\mathrm{P} = \left(1 - \frac{\rho}{\rho_s}\right) \tag{1}$$

where, ρ and ρ_s stand for the density of aerogel and solid materials, respectively. ρ_s was calculated based on the solid density of cellulose, CNTs and GNPs according to Eq. 2 (Zhang et al. 2021).

$$\rho_s = \frac{1}{\frac{mcell}{\rho cell} + \frac{mCNTs}{\rho CNT} + \frac{mGNP}{\rho GNP}} \quad (2)$$

where, *mcell, mCNTs and mGNP* are the mass fractions of cellulose, CNT and GNP, respectively. ρ_{cell} is the density of the cellulose (1.59 gcm^{-3}), ρ_{MWCNT} is the density of CNT (2.4 gcm^{-3}) and ρ_{GNP} is the density of GNP (2.3 gcm^{-3}).

To investigate structural properties and determinate the variation functional groups of samples were characterized by Raman spectroscopy (Raman, WITEC ALPHA, 3100R in the range of 800–2000 cm^{-1}) and by Fourier transform infrared spectroscopy analyzer (FT-IR, Perkin- Elmer 1725 at scan resolution of 4 cm^{-1} in the range of 500–4000 cm^{-1}). The crystalline structure of the samples was illuminated using X-ray diffractometer (XRD, Malvern Panalytical Empyrean) with Cu-K α radiation, 1.5418 A ° at 45 kV and 40 mA, in the range of 5–60°. The XRD peaks were fitted using Gaussian function using Origin(Pro), Version 2018. OriginLab Corporation, Northampton, MA, USA to acquire peak position, peak height and the full width at half-maximum (FWHM) for samples. The microstructure morphology of samples was investigated using a scanning electron microscope (SEM) (JEOL SEM 7100 EDX) at 20 kV. The electrical conductivity of was obtained at room temperature according to ASTM F43-99 by a four-point probe unit (Four Point Probe-Entek Electronics).

The EMI SE of the samples was examined via an Anritsu MS2028C VNA master vector network analyzer was operated to survey EMI SE with a WR-90 waveguide for X-band measurements (8.2–12.4 GHz). The rectangular samples (22.86 mm × 10.16 mm) were mounted inside a sample holder, which was centralized between the wave-guide's flanges. The scattering parameters (S_{11}, S_{12}, S_{21}, and S_{22}) of the samples were evaluated in the X-band frequency (8–12 GHz). The power coefficients were calculated according to the following Eq. 3–5 (Ma et al. 2023):

$$R = \left|S_{11}^2\right| \quad (3)$$

$$T = \left|S_{21}^2\right| \quad (4)$$

$$1 = A + R + T \quad (5)$$

where A, R and T show absorption, reflection and transmission coefficient, respectively. The EMI shielding ability is used to assess with total EMI shielding SE_T, absorption SE (SE_A), reflectance SE (SE_R), and microwave multiple internal reflection SE (SE_M, which can be negligible when $SE_T \geq 15$ dB), which are computed from power coefficients according to the following Eqs. (6)–(8) (Guo et al. 2020b; Zong et al. 2022a):

$$SE_R(dB) = 10 * \log\left(\frac{1}{1-R}\right) \quad (6)$$

$$SE_A(dB) = 10 * \log\left(\frac{1-R}{T}\right) \quad (7)$$

$$SE_T(dB) = 10 * \log\left(\frac{1}{T}\right) \quad (8)$$

Results and discussion

Density and porosity properties of RCA aerogel and CxGy aerogels

RCA and composite aerogel produced via ambient drying which is the low cost, facile and effective route to manufacture aerogels. In this study, cellulose and nanofiller disperse in NaOH/urea system and colloid molded at a freezing temperature of − 18 °C. Then obtained hydrogels solvent exchanged in ethanol bath and drying under the ambient (Mai et al. 2024). Cellulose was dissolved in the NaOH/urea solution to break hydrogen bond between cellulose chains (Liu et al. 2016). Moreover, urea inhibited the accumulation of cellulose chains at a freezing temperature of − 18 °C forming aerogels with improved porosity (Sankhla and Neogi 2024). After the incorporating of oxygen group containing GNP and carboxylic functionalize MWCNT (Damnalı and Eskizeybek 2019), hydrogen bonds could be created between carbon nanofiller's oxygen-containing groups and hydroxyl groups of cellulose (Liu et al. 2016). Also, hydrogen bond formation accelerated the cellulose solution's gelatinization. (Long et al. 2019). During the freezing of aqueous colloids, water molecules repulsed each other, increasing their volume and forming low-density and loose crystals. Meanwhile,

cellulose and MWCNT: GNP were trapped in the gaps of the irregularly growing ice crystals, resulting in the formation of cellulose carbon hybrid structures (Wu et al. 2023b). Subsequently, frozen hydrogels were immersed in ethanol, which has a lower freezing point than water; water and ethanol were rapidly displaced. Moreover, the low surface tension ethanol further increased the hydrogen bonding force, resulting in a robust aerogel structure and ensuring that the aerogel skeletal structure did not collapse during ambient drying (Wu et al. 2023b; Xu et al. 2023) (Fig. 2a, Fig. S1a). In contrast, when frozen hydrogels were immersed in water, the high surface tension of water-soluble cellulose and water disrupted the cellulose structure, causing the hydrogel to disintegrate and the aerogel structure to collapse. (Fig. S1b). In addition, the robust hydrogen bonding interactions between matrix and nanofiller increased the microstructural stability of aerogels (Yang et al. 2022) (Fig. 2b, Fig. S1c). Also, these aerogels could sustain a load 3500 times its own weight without deformation (Fig. 2c).

The lightweight properties of aerogels were given in Fig. 2d and Table 2. Depending on production methods, the density of cellulose aerogels ranges from 0.005 to 0.2 gcm^{-3} (Prasad et al. 2024). Generally, ultra-low-density cellulose aerogels are manufactured with supercritical or freeze-drying methods (Al Abdallah et al. 2024; Wang et al. 2024b). Unfortunately, these techniques are not scalable as they require special requirements and consume high energy. The density of RCA produced with scalable ambient drying is 0.064 gcm^{-3} with 95.78% porosity. As the carbon nanofiller was added to the cellulose aerogel skeleton, the density of hybrid aerogels increased to 0.088, 0.094, and 0.087 gcm^{-3} for C7G0, C0G7, and C7G7, respectively. The lightweight C7G7 aerogel stand on taraxacum officinale without bending (inset Fig. 2d). According to Fig. 2 and Table 2, the samples can fulfill the lightweight advantages of aerogels with low density and high porosity.

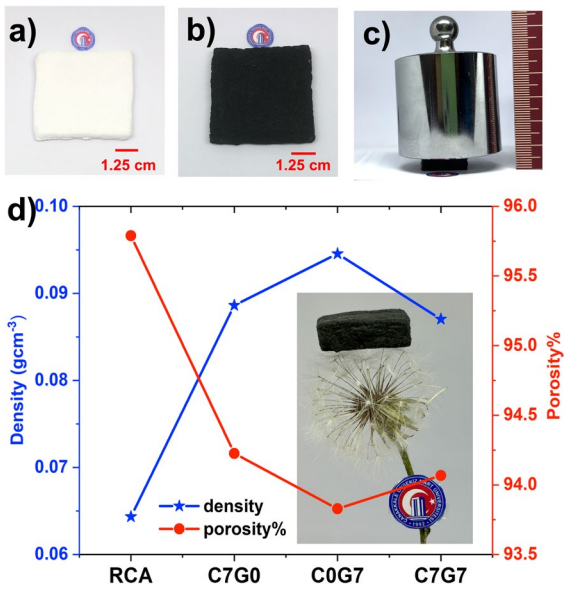

Fig. 2 The photographs of **a** RCA and **b** C7G7 composite aerogels in square shape **c)** C7G7 sustaining an item 500 g weighing **d** density and porosity% of RCA, C7, G7 and C7G7 samples (inset C7G7 on taraxacum officinale)

Table 2 Density and porosity properties of samples

Sample code	Density (gcm^{-3})	Porosity %
C3G0	0.072	95.36
C3G3	0.079	94.87
C3G7	0.082	94.53
C3G10	0.085	94.17
C7G0	0.088	94.22
C7G3	0.081	94.60
C7G7	0.087	94.06
C7G10	0.086	93.99
C10G0	0.078	94.78
C10G3	0.078	94.68
C10G7	0.079	94.48
C10G10	0.102	92.73
C0G3	0.085	94.54
C0G7	0.094	93.82
C0G10	0.093	93.78
RCA	0.064	95.78

Structural analyses

Both bacteria and plants can produce cellulose, a linear polymer made up of repeating glucose residue units joined by β-glycoside bonds at carbons one and four (Salem et al. 2023). Figure S2 depicts the chemical structure of cellulose (French 2017). Different polymorphic forms can be found in cellulose, a semi-crystalline biopolymer with ordered crystalline and disordered amorphous areas (Nishiyama et al. 2002; Rodríguez-Fabià et al. 2022). The

most common crystal structure in nature is cellulose I, which is mostly found in plants and can change into different polymorphs through a variety of processes. Another crystal structure created by cellulose I's regeneration under alkaline conditions is cellulose II (Langan et al. 2001). The efficiency assessment of recycling process was examined according to Eq. (S1)–(S3). The efficiency of recycling processes of OWP was given in Table S1. The elimination of impurities led to an elevated degree of hydrolysis efficiency. The elevated percentage of hydrolysis efficiency evidences the effective execution of the acid hydrolysis process. The hydrolysis process has succeeded (Najafabadipoor et al. 2025) with a hydrolysis efficiency of 71.68% in the current study. Process efficiency is known as the amount of material generated from the entire raw sample. The efficiency of the process in this study was determined to be 42.83%. The elimination of impurities, hemicellulose, lignin, and even minimal cellulose content leads to a reduction in process efficiency.

To investigate the structural properties of samples, Raman spectroscopy, which is a useful way to examine the existence of carbon nanofillers and their possible interactions in a matrix. Figure 3a shows the Raman spectrum of the RCA, C7G0, C0G7 and C7G7 in the range of 250–2000 cm^{-1}. The proportion of cellulose II can be calculated using Eq. (9) (Agarwal et al. 2021), which compares the intensity of the 577 cm^{-1} peak (I_{577}), specific to the cellulose II polymorph, with the intensity of the peaks at 1096 cm^{-1} (I_{1096}) found in both cellulose I and cellulose II.

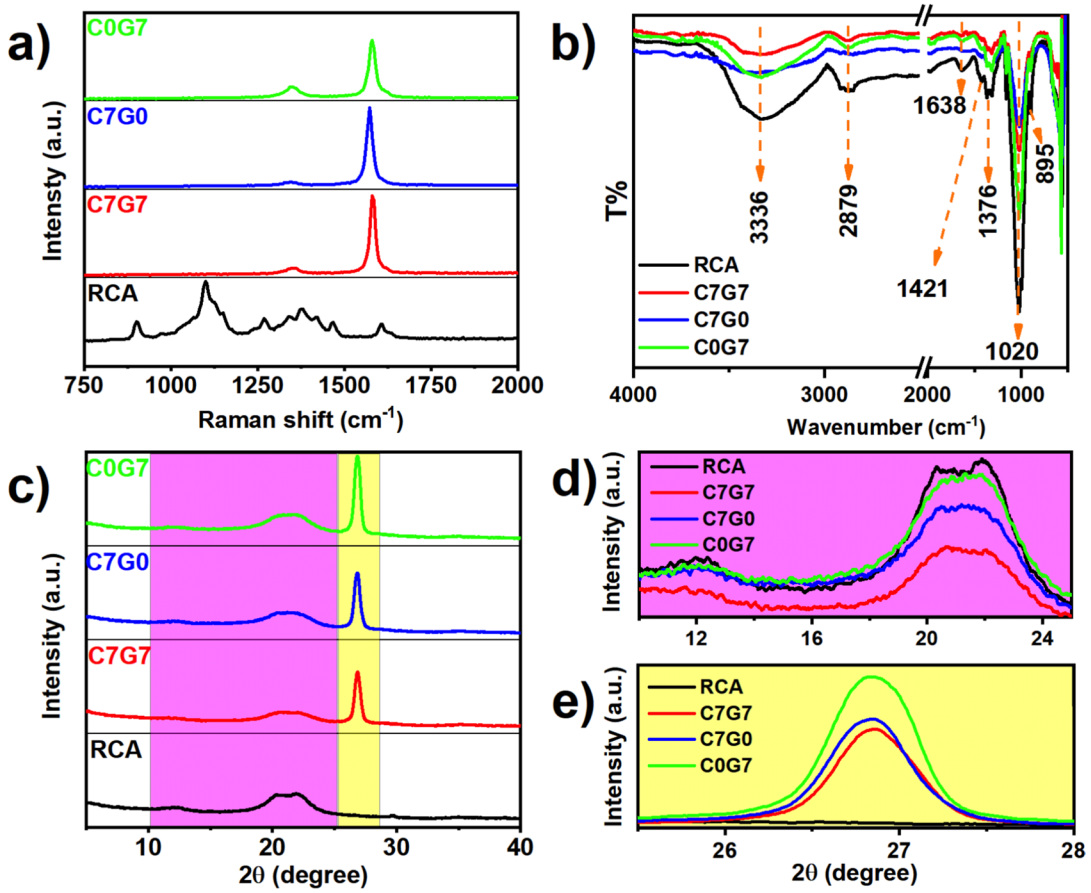

Fig. 3 **a** Raman spectra**, b** FTIR spectra, XRD pattern in the range of **c** 5–40 2θ (degree), **d** 11–25 2θ (degree) and **e** 25.5–28 2θ (degree) of the RCA, C7G0, C0G7 and C7G7 aerogel

$$\text{Cellulose II\%} = \left[\frac{\frac{I_{577}}{I_{1096}} - 0,009}{0,0017} \right] \quad (9)$$

The Raman spectra revealed that the intensity of I_{577} was measured at 19.08, whereas the intensity of I_{1096} was measured at 199.74. According to Eq. (9), Cellulose II % conversion was calculated as 50.89%. The Raman spectrum of C7G0, C0G7 and C7G7 depicted two characteristic peak of GNPs and CNTs at around 1300 cm^{-1} and 1500 cm^{-1}. The D band which is located at 1248–1352 cm^{-1} is related the defects in graphitic structure and disordered carbon, the G band (1572–1580 cm^{-1}) arises from the crystalline graphitic and vibrations of sp^2 carbon. The ratio of I_D and I_G is a value for evaluating the defects of graphitic structure. The low I_D/I_G ratio reflects the high order degree of graphitic structure (Pandit et al. 2023). Damnalı and Eskizeybek reported the I_D/I_G ratio as 0.4 and 1.01 for GNPs and CNTs from the same manufacturer, respectively (Damnalı and Eskizeybek 2019). Two peaks were found for composite aerogels compared to those of supplied GNPs and CNTs which indicated that there is no obvious destruction of carbon structures during the dissolution-regeneration process (Ma et al. 2021). The extremely low I_D/I_G ratio of C7G0, C0G7 and C7G7 composite aerogels, calculated as 0.16, 0.04, and 0.03, respectively, indicate the CNTs/GNPS was preserved upon their incorporation the cellulose matrix (Choi et al. 2024). Furthermore, C7G7 show low I_D/I_G ratio which may be related due to the hydrogen bonding between carbon nanostructures and cellulose matrix (Saini et al. 2009).

To complete structural characterization and reveal the functional groups, the FTIR spectra of samples were recorded, and the results were given in Fig. 3b. The 3336 cm^{-1} and 1638 cm^{-1} peaks correspond to the –OH group stretching in cellulose and adsorbed water. The peak at 2879 cm^{-1} was assigned to the C–H group in glucose in polysaccharide ring cellulose. The shoulder shape peak at 1421 cm^{-1} and the sharp peak at 1020 cm^{-1} are due to the symmetric bending of -CH_2 and –C–O–C vibration of the pyranose ring, respectively (Chen et al. 2018). Also, the peak at 895 cm^{-1} arose from the β- glycosidic linkages (C–H and O–H bending). As shown in Fig. 3b, the characteristic peaks of cellulose are completely retained after nanofiller modification. However, the peaks shifted in high wavenumbers, and the peak intensities decreased due to the interaction of cellulose and carbon-based nanofiller (Haspulat Taymaz 2023; Jyothibasu et al. 2019; Wulandari et al. 2016).

The crystalline structure of the samples was examined via the XRD method, and the XRD patterns are given in Fig. 3c–e. The diffraction peaks at 2θ = 12.1, 20.5, and 22.4° with Miller indices of 1–10, 110 and 020, respectively, result in the cellulose II crystalline allomorph (Fig. 3c, d) (French 2014). Moreover, these diffraction peaks prove the transformation from cellulose I to cellulose II during regeneration (Zhou et al. 2024). In Fig. 2d, the diffraction peak intensity at around 2θ = 12.4 and 22.4° declined with decreasing cellulose amount in the composite aerogel matrix due to the addition of the carbon-based nanofiller. Moreover, a slight shift occurred in the 22.4° peak towards a smaller diffraction angle with the addition of a carbon-based nanofiller. This shift could be attributed to residual tensile stress from forming hydrogen bond cross-linking between the cellulose and the carbon nanofiller (Damnalı and Eskizeybek 2019) (Fig. 3c, e). Furthermore, a new additional sharp peak was observed at around 2θ = 26.8°. In the XRD pattern of C7G0 composite aerogel, the peak centered at 2θ = 26.82° with Miller indices of 002 strongly confirms CNT crystal structure (Atchudan et al. 2015; He et al. 2020). Similarly, the diffraction peak centered at 2θ = 26.84 with Miller indices of 002 addresses the GNP crystal structure (Batakliev et al. 2021; Liu et al. 2019; Rashad et al. 2017). The XRD pattern of C7G7 is similar C7G0 and C0G7, but the diffraction peak regarding the carbon structure was expanded due to increasing the crystalline size. These results show an interaction between carbon nanofiller and cellulose structures (Wang et al. 2017). Also, the slight shifting in the peak positions may be ascribed to charge transfer interactions between cellulose and CNT/GNP (Saini et al. 2009).

The crystalline size (D) of RCA, C7G0, C0G7 and C7G7 aerogel was calculated by using Scherrer equation (Scherrer 1918):

$$D = \frac{0.94.\lambda}{\beta.\cos(\theta)} \quad (10)$$

where λ, θ and β were symbolized by X-ray wavelength, Bragg angle, and the full width of the

diffraction line at half the maximum intensity. According to Eq. 10, the values of D for RCA, C7G0, C0G7, and C7G7 perpendicular to their (020) lattice planes is about 3.69, 2.41, 2.57 and 5.05 nm. The peak positions and corresponding FWHM values for lattice planes are given in Table 3.

Also, the crystallinity properties of samples were identified via crystallinity index (CrI%) with the Segal et. al. (1959) peak height method by using Eq. (11):

$$\mathrm{CrI\%} = \frac{I_{020} - I_{am}}{I_{020}} \times 100 \tag{11}$$

where I_{020} and I_{am} are the intensity of the 020 lattice peak and amorphous ($2\theta = 16°$) (Nomura et al. 2020), respectively. Fig S3 shows the determination of peak heights of the 020 lattice peak and amorphous for RCA sample. The CrI% values of samples are given in Table 3.

Morphological analysis

The microstructure of the RCA and CxGy aerogels are shown in Fig. 4. RCA has a porous 3D network matrix, and individual cellulose fibers are circular rodlike structure with the diameter of approximately 7 µm. This 3D network structures are observed in also C7G0, G0C7 and C7G7 aerogel. In the SEM images of C7G0 and C0G7 aerogels, CNTs and GNPs were grafted on the individual cellulose fiber, respectively. The SEM images of C7G7 aerogel indicates grafted cellulose fibers with CNTs and GNPs nanofillers and the conductive network is visible in between the cellulose fibers.

Electrical conductivity

Electrical conductivity experiments were performed using the four-point electrical conductivity method to investigate the impact of nanofiller type, quantity, and synergistic effect on the conductivity properties. Figure 5a shows the electrical conductivity values versus nanofiller type and amount. As can be seen from the figure, as the ratio of MWCNT and GNP in the network increases, the electrical conductivity increases. The electrical conductivity was calculated to be 0.0021 S/cm when CNTs (7%wt.) was introduced to the cellulose aerogel network structure, and it was measured to be 0.0028 when 7% (wt.) GNPs was added to the medium. The increased electrical conductivity indicates that the carbon structures are homogeneously distributed in the cellulose matrix, forming conduction pathways. Moreover, when CNTs and GNPs (7:7; %wt.) were combined, the electrical conductivity was calculated as 0.04326 S/cm, almost 200 times higher than when added individually. The synergistic effect of combining 1D and 2D carbon structures to provide more electrical conduction routes may cause a further increase in electrical conductivity (Huang et al. 2022b). The conductivity values of all samples are given in Table S2. The electric conductivity of was tested using a circuit constructed with the RCA (Fig. 5b) and C7G7 (Fig. 5c) aerogel samples. When the electrically nonconductive RCA sample is connected to the circuit, the LED lamp does not light. However, when the circuit is completed with the electrically conductive C7G7, the LED lamp illuminates.

Thermal properties

The thermal properties of RCA and C7G7 hybrid aerogel were investigated via DSC method. The DSC curves of RCA and C7G7 are given in Fig. 6a. The

Table 3 The peak positions, FWHM values and crystallinity (%) of samples

Sample	Peak positions (2 θ°)	FWHM (°)							CrI%
	1–10	110	020	002	1–10	110	020	002	
RCA	12.11	20.58	22.40	–	1.790	3.005	2.291	–	70.8
C7G0	12.10	18.85	21.39	26.82	1.892	5.393	3.502	0.568	57.4
C0G7	12.10	20.00	21.51	26.84	2.162	4.517	3.290	0.569	60.9
C7G7	12.02	20.97	22.41	26.84	2.124	3.465	1.675	0.563	64.0

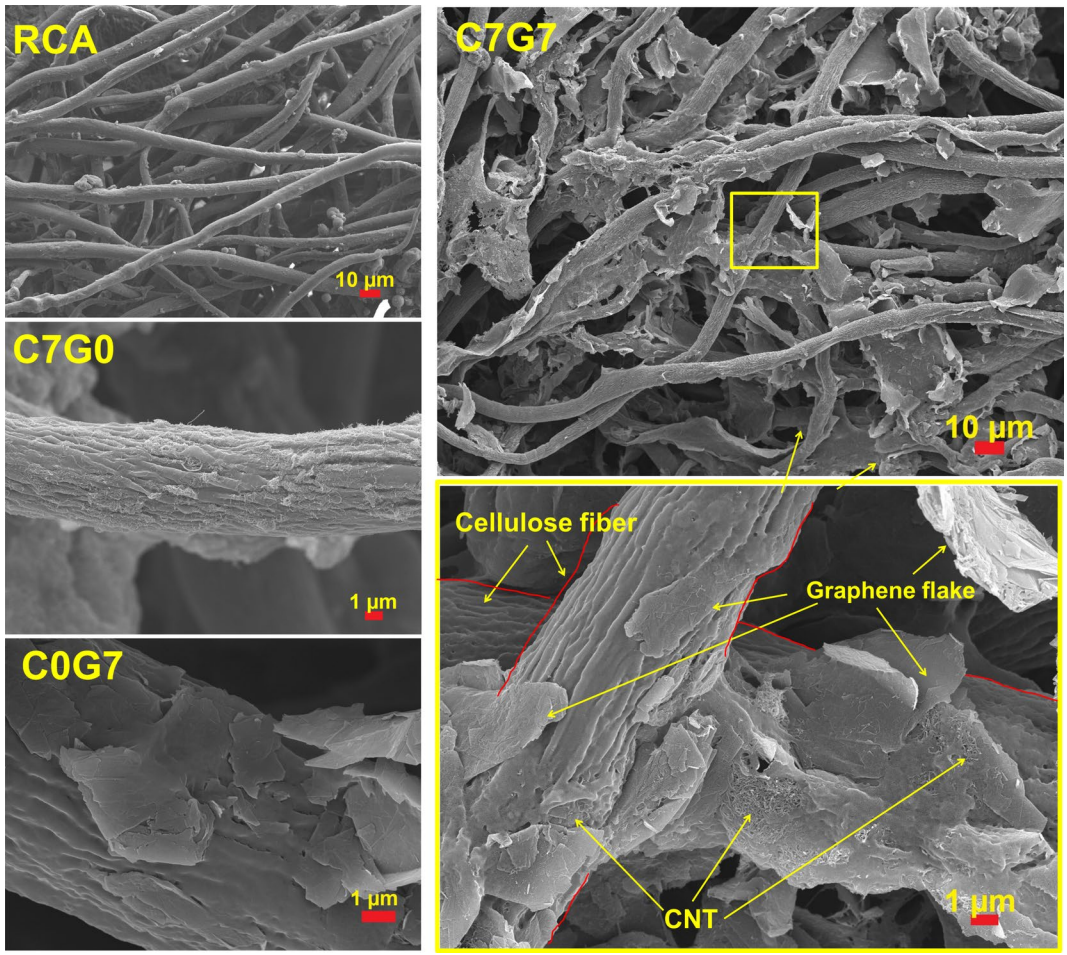

Fig. 4 SEM images of RCA, C7G0, C0G7 and C7G7 aerogels

observed first broad peak at 51 °C and 79 °C display the dehydration of the samples. The peaks appearing at 377 and 382 °C indicate the melting temperature (T_m) of RCA and C7G7, respectively. Introducing MWCNT: GNP carbon hybrid structures into the cellulose skeleton leads to a notable increase in Tm. The carbon hybrid structures promoted the strengthening of hydrogen bonds and increased crosslinking, which enhanced the thermal stability of the hybrid aerogel. Moreover, DSC results, in line with the XRD data, suggest that a rise in crystallinity necessitates more heat for the melting process, thereby increasing Tm (Zhang et al. 2024a; Zheng et al. 2002). The thermal conductivity increases with the addition of thermally conductive carbon structures in 3D network structures (Lee and Kim 2022; Zhang et al. 2023). In this regard, to get an idea about the thermal conductivity performance of the produced aerogel samples, a laboratory scale method was used (Zhou et al. 2019). As shown in Fig. 6b, the 5 mm thick sample was placed on a hot surface at 100 ℃. The change in surface temperature during the heating process was recorded instantaneously with an infrared thermometer, and the temperature data obtained is given in Fig. 6b as a function of time. RCA reaches a maximum of 70℃ in 10 min, while the C7G7 sample reaches 90℃ in 1 min, suggesting that the C7G7 sample has relatively higher thermal conductivity than RCA.

EMI shielding performance

The average EMI SE_T values of CxGy aerogel samples with different MWCNT: GNP loading in the X-band frequency (8.2–12.4 Ghz) were given in

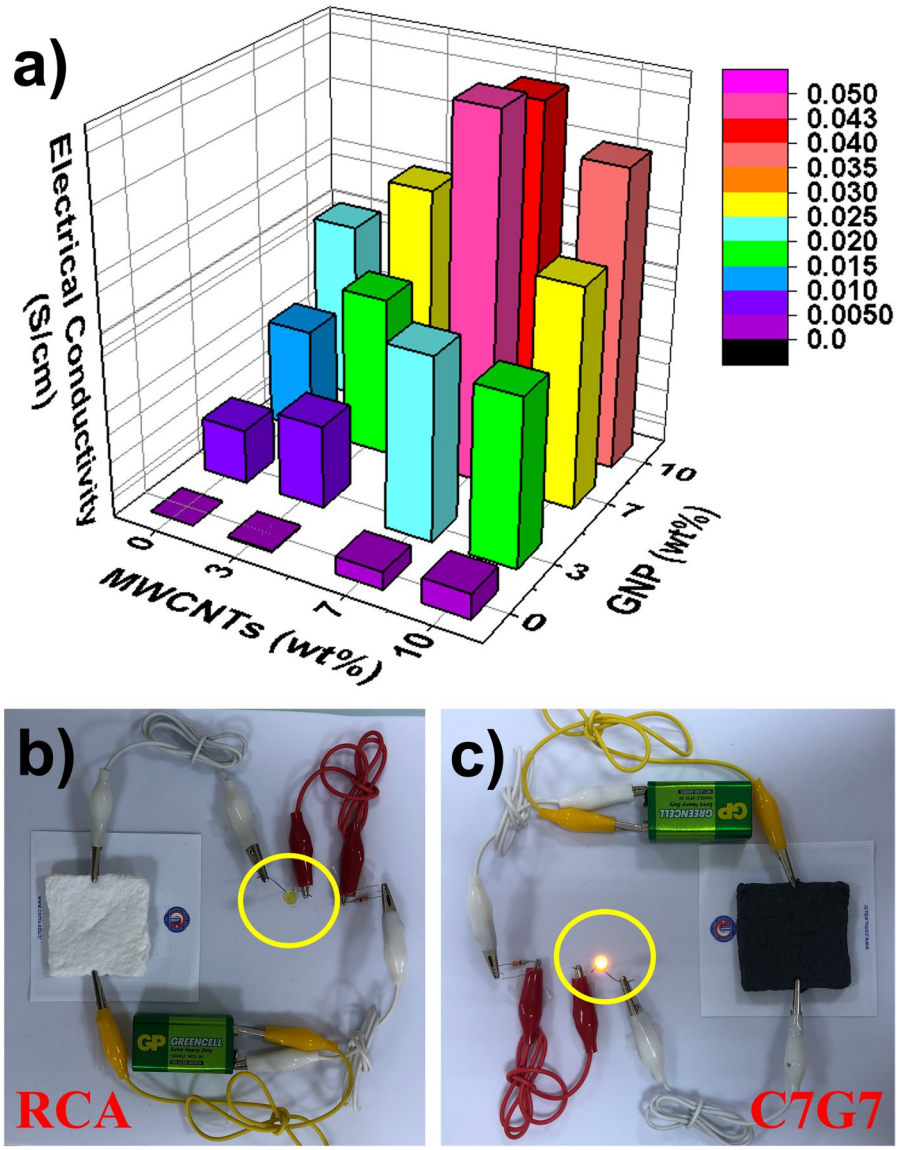

Fig. 5 **a** Electrical conductivities of aerogel samples and a circuit constructed with the **b** RCA and **c** C7G7 aerogel

Fig. 7a. With rising carbon nanostructures in the cellulose matrix, the average EMI SE_T is increased due to the increasing of electrical conductivity (Han et al. 2021; Li et al. 2022b; Zhang et al. 2024c) The C7G7 aerogels with 14% (CNTs:GNPs, 7:7 (wt.,wt.) nanofillers have the highest average EMI SE_T of 32 dB. Similarly, the EMI SE_A values of the sample increased with the rising carbon nanofiller loading. Moreover, the synergetic interaction between CNTs and GNPs in the cellulose matrix is important in increasing the EMI SE_A values. The EMI SE_A values of C7G7 and C10G10 are 28.84 and 29.90 dB, respectively. The average EMI SE_A, SE_R and SE_T values are given in Table S3.

Figure 7c shows the variation of EMI SE versus frequency of C7G7 aerogel with 14% (wt.) nanofiller at the thickness of 2 mm and density of 0.087 gcm^{-3} at the X band. The EMI SE_T values of C7G7 aerogel far exceed the desired SE_T value of 20 dB for business applications at whole X-band frequency (Yang et al. 2025). Moreover, the maximum EMI SE_T value of 40.2 dB was obtained at 8.92 GHz. Also, the EMI SE_T and SE_A curves of C7G7 aerogel are relatively close. The EMI SE_A was measured as 33.4 dB at

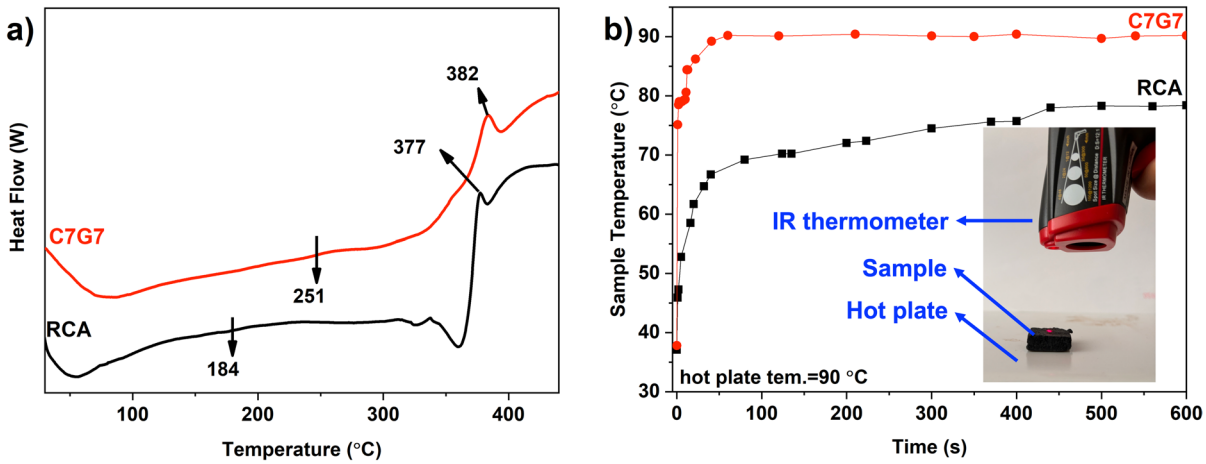

Fig. 6 **a** DSC thermograms of RCA and C7G7 samples, **b** time-dependent temperature profile of the top surface of RCA and C7G7 after placing on a 100 °C hot plate. The inset shows a photograph of the measurement apparatus

8.92 GHz. Also, the EMI SE_R values are less than 10 dB whole X-band frequency. The EMI SE_R curves of the C7G7 samples exhibit a zigzag pattern between negative and positive values, indicating a diminished response capability related to the reflectance mechanism as frequency varies (Yıldırım 2023).

Dielectric loss increases when nonconductive materials and conductive fillers possess distinct electrical conductivities. This mismatch between electrical conductivity causes polarization and/or charge accumulation at the interfaces. Because of their many interfaces resulting from the matrix–nanofillers and nanofillers–nanofillers, the hybrid aerogels are caused mainly by the absorption of EMWs (Lee et al. 2022; Wang et al. 2021). This study used sustainable cellulose as a matrix by adding the CNTs/GNPs hybrid nanofillers to shield EMI waves. Cellulose matrix can suppress EM radiation through adsorption, reflection, or multiple reflections. The conductivity mismatch at the interfaces between CNTs/GNPs nanofillers and cellulose matrix increase interfacial polarization loss. The conductive CNTs/GNPs network functions as a dissipative medium for mobile charge carriers and the partial transformation of electromagnetic energy into thermal energy (Vendange and Flavin 1996; Zhang et al. 2024d). The increase of conductive networks may result in enhanced EMI dissipation through absorption (Kruzelak et al. 2021). In addition, thanks to the porous structure provided by the cellulose matrix the transmission path of EMWs is extended by multiple scattering (Wang et al. 2021).

To deeply analyze the EMI shielding mechanism of C7G0, C0G7, and C7G7 aerogels, the A, R, and T coefficients were calculated from Eq. 3–5, and the results were given in Fig. 7d. The A and R coefficients of C7G0 are 0.89 and 0.09. C7G0 with low electrical conductivity (Fig. 5a and Table S2) demonstrates a reflectance-dominated EMI character. However, the A coefficient increased acutely with the addition of GNP nanostructures to the aerogel matrix and the direct opposite sight for the R coefficient. The conduction pathways and electron percolation are formed by adding GNP to the aerogel matrix (Lee et al. 2022). As expected, the CNTs/GNPs hybrid carbon nanostructures promote a rise in multiple interfaces due to their hierarchical structure. Consequently, C7G7 aerogel exhibits absorption-dominant EMI shielding characteristics with an A coefficient of 0.510.

Figure 7e schematizes the EMI shielding mechanism of CNTs/GNPs doped recycled cellulose aerogel. The EMI shielding material attenuates the incident EMWs by reflection and absorption. Due to a large number of free electrons on the surface of the CNTs and GNPs, some incident waves are immediately reflected (Guo et al. 2020a). The shielding property of composite aerogel is due to its high electrical conductivity owing to the conductive nanofillers. In addition, another possible EMI shielding mechanism is that when EMWs enter the composite aerogel, they are attenuated by dielectric loss due to the mismatch between the electrical conductivity of the cellulose

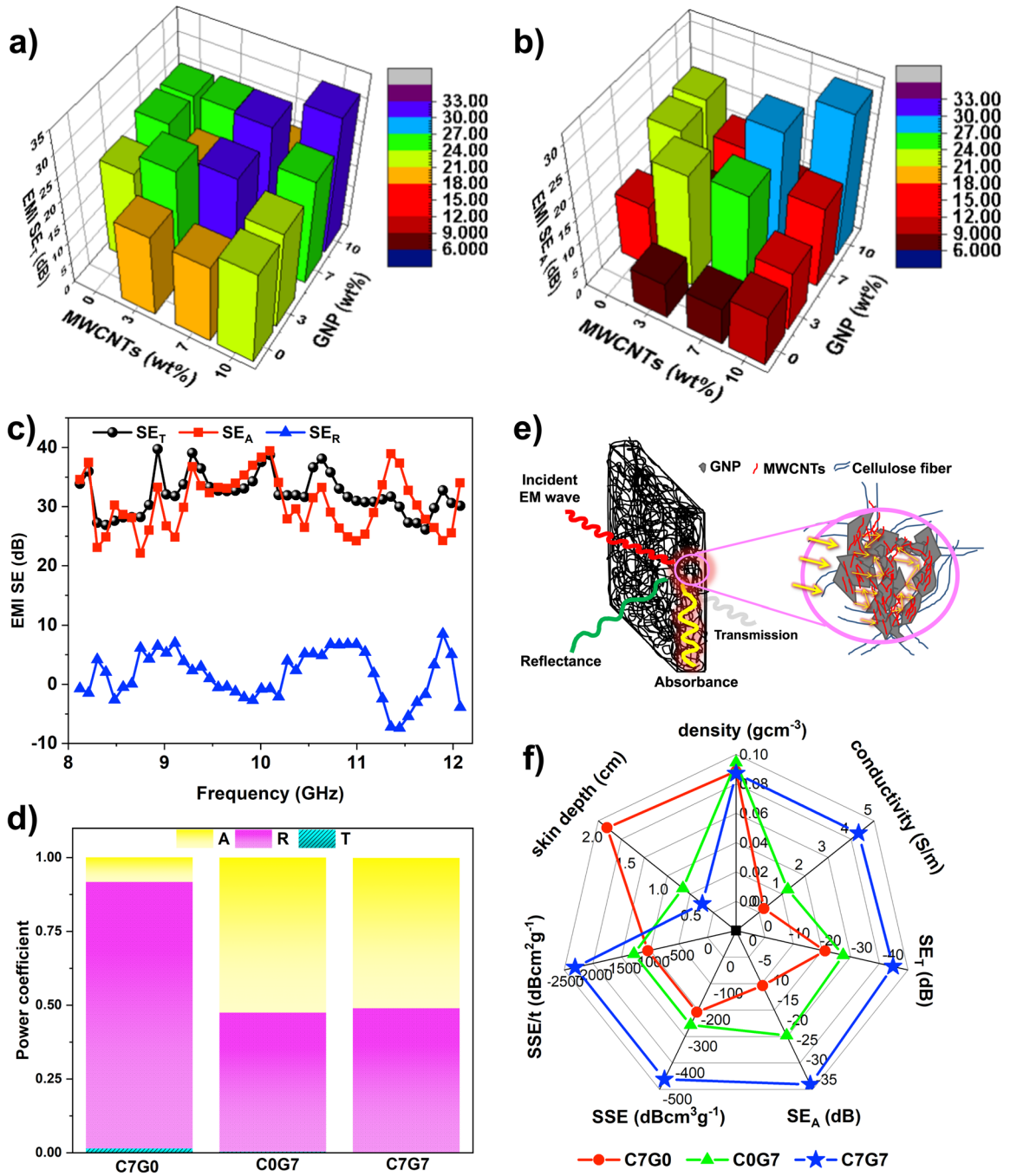

Fig. 7 The comparison of average EMI **a** SE_T and **b** SE_A values of produced CxGy aerogel samples, **c** Variation in EMI SE_T, SE_A and SE_R as a function of frequency for the C7G7, **d** EMI-shielding coefficient of the composites, **e** Schematic illustrations of the EMI-shielding mechanisms for the C7G7 **f** Radar chart for comparison of density, porosity, SE_T, SE_A, skin depth, SSE, SSE/t

matrix and the hybrid carbon structures (Guo et al. 2023a; Wang et al. 2022) and the partial transformation of electromagnetic energy into thermal energy (Vendange and Flavin 1996; Zhang et al. 2024d). Meanwhile, the hierarchical structures of CNTs/GNPs carbon structures facilitate multiple scattering and provide additional interfaces (Zheng et al. 2024). At the same time, the irregular pores provided by the cellulose matrix ensure effective aerogel dispersion of incident EMWs. Thus, the EMWs are secondarily attenuated at the interfaces provided by the CNTs/GNPs hybrid carbon structures and the pores provided by the cellulose matrix. In this way, the conductive aerogel structure exhibits an absorption-dominated EMI character (Guo et al. 2023b).

Both the enhancement of thickness and conductivity of materials make favorable contribution of the overall EMI shielding performance by the following Eq. (12):

$$SE_T = 50 + 10.\log(s/f) + 1.7t((s.f)^{0.5} \quad (12)$$

where σ, f and t represent the electrical conductivity, frequency and the thickness of the EMI shielding of material, respectively. So, to eliminate the effect of the dimension of the materials on the EMI shielding effectiveness, specific (SSE in $dBcm^3g^{-1}$) and absolute (SSE/t in $dBcm^2g^{-1}$) shielding efficiencies should be calculated. The SSE and SSE/t values are given critical information about the relationship between shielding efficiency and density or thickness.

Also, the skin depth of the materials is another important parameter which affects the shielding performance. It can be defined as the distance required for the EMWs to attenuate to 1/e of the incident power. The skin depth of the materials can be calculated as Eq. 13 (Chung and Ozturk 2022; Oliveira et al. 2023).

$$SE_A = 20\log e^{t/\delta} = 20\log(e) = 8.69\left(\frac{t}{\delta}\right) \quad (13)$$

where t and δ represent the EMI shielding material's thickness and skin depth. Therefore, EMI SE_T can be expressed as (Li et al. 2018):

$$SE = 50 + 10.\log(s/f) + 8.69\left(\frac{t}{\delta}\right) \quad (14)$$

Thus, the SE_T of C7G7 was estimated using Eq. (14) to compare with the experiment results. In Fig. S3, the predicted EMI SE displays a similar trend to the experiment results. However, the difference between the predicted and experimental results exhibits differences in some frequencies. It may be related the due to neglecting the term of SE_M in Eq. (14) (Li et al. 2018).

To identify the relationship between density, conductivity, SE_T, SE_A, SSE, SSE/t and skin depth values, radar chart is given in Fig. 7e. As expected, as the conductivity of aerogel samples is increased, the SE_T and SE_A increase. The skin depth of C7G0 and C0G7 are calculated as 1.96 and 0.81 mm which are less than the thickness of testing sample (2 mm). Moreover, as CNTs and GNPs loading simultaneously, the skin depth decreases to 0.51 mm, which is mainly attributed to the enhanced electrical conductivity due to the higher conductive nanofiller weight and synergetic effect (Zong et al. 2022a). Table 4 show that compared to most porous materials (Fu et al. 2022; Huang et al. 2022b; Li et al. 2022c; Liang et al. 2019; Park et al. 2021; Tan et al. 2018; Yang et al. 2020), the C7G7 aerogel possesses notably low density and high SSE and SSE/t values. As CNTs and GNPs load simultaneously to the cellulose aerogel skeleton, its SSE and SSE/t values significantly increase. At a density of 0.087 gcm^{-3}, C7G7 shows an exceptionally high SSE value of 461.95 $dBcm^3g^{-1}$ and an SSE/t value of 2309.29 $dBcm^2g^{-1}$. These results imply that the C7G7 aerogel can meet the lightweight and high-efficiency EMI shielding requirement.

Conclusion

Cellulose aerogels were produced using cellulose from wastepaper pulp using sustainable, scalable and facile method without the need for special equipment. Lightweight and porous aerogel with electrical conductivity were developed by adding CNTs and GNPs nanostructures to the cellulose aerogel matrix. Due to the synergistic effect between CNTs and GNPs and the interaction between hybrid carbon nanofiller and cellulose matrix, the capability of absorption EMWs has increased and shows superior EMI SE at the X band. The effect of nanofiller amount and type on physical properties, electrical conductivity and EMI shielding effectiveness were investigated. The mismatch

Table 4 Comparison of physical properties and EMI SE_T, SSE and SSE/t of C7G7 aerogel with other literature works

Samples	Density (gcm^{-3})	Thickness (mm)	Nano-filler (wt.%)	SET (dB)	SSE ($dBcm^3g^{-1}$)	SSE/t ($dBcm^2g^{-1}$)	References
CNT/cellulose-BN/PVA	0.275	2	25.4	29.8	108.36	541.81	(Zhang et al. 2024b)
CANF/CNT-750	0.12	0.024	70	35.95	299.58	124,826.38	(Fu et al. 2022)
CCA50	0.0519	2	50	23.69	456.45	2282.27	(Huang et al. 2022b)
WWCF/GNP15	–	0.28	15	43	–	–	(Park et al. 2021)
GNP/RGO/EP	–	3	30.5	51	–	–	(Liang et al. 2019)
PASS/GNP	–	2	5	41	–	–	(Yang et al. 2020)
MG3:7	1.73	0.04	50	36.2	20.92	5231.1	(Li et al. 2022c)
GNP/B4C	2.57	1.5	2	40	15.56	103.76	(Tan et al. 2018)
C7G7	0.087	2	14	40.2	461.95	2309.29	This work

between the electrical conductivity of the cellulose matrix and the hybrid carbon structures increases the dielectric loss when EMWs enter the composite aerogel. CNTs/GNPs carbon structures simplified multiple scattering by ensuring extra interfaces. The pores provided by the cellulose matrix ensure effective dispersion of incident EMWs in aerogel. The lightweight C7G7 shows an exceptionally high SSE value of 461.95 $dBcm^3g^{-1}$ and an SSE/t value of 2309.29 $dBcm^2g^{-1}$. These findings suggest that the C7G7 aerogel can meet the lightweight and high-efficiency EMI shielding requirement.

Acknowledgments The authors acknowledge funding support from The Scientific and Technical Research Council of Türkiye under grant number 121C507.

Author contributions Bircan Haspulat Taymaz: Conceptualization, investigation, methodology, formal analysis, data curation, writing—review&editing, project administration, funding acquisition Volkan Eskizeybek: Conceptualization, investigation, methodology, writing—review&editing, supervision.

Funding Open access funding provided by the Scientific and Technological Research Council of Türkiye (TÜBİTAK).

Data availability No datasets were generated or analysed during the current study.

Declarations

Conflict of interest The authors declare no competing interests.

Ethical approval This paper does not involve any human or animal experiments. Not applicable.

Consent for publication Not applicable.

References

Agarwal UP, Ralph SA, Baez C, Reiner RS (2021) Detection and quantitation of cellulose II by Raman spectroscopy. Cellulose 28:9069–9079. https://doi.org/10.1007/s10570-021-04124-x

Akhlamadi G, Goharshadi EK (2021) Sustainable and superhydrophobic cellulose nanocrystal-based aerogel derived from waste tissue paper as a sorbent for efficient oil/water separation. Process Saf Environ Prot 154:155–167. https://doi.org/10.1016/j.psep.2021.08.009

Al Abdallah H, Tannous JH, Abu-Jdayil B (2024) Cellulose and nanocellulose aerogels, their preparation methods, and potential applications: a review. Cellulose 31:2001–2029. https://doi.org/10.1007/s10570-024-05743-w

Atchudan R, Pandurangan A, Joo J (2015) Effects of nanofillers on the thermo-mechanical properties and chemical resistivity of epoxy nanocomposites. J Nanosci Nanotechnol 15:4255–4267. https://doi.org/10.1166/jnn.2015.9706

Batakliev T et al (2021) Physico-chemical characterization of PLA-based composites holding carbon nanofillers. Appl Compos Mater 28:1175–1192. https://doi.org/10.1007/s10443-021-09911-0

Chen W, He H, Zhu H, Cheng M, Li Y, Wang S (2018) Thermo-responsive cellulose-based material with switchable wettability for controllable oil/water separation. Polymers (Basel). https://doi.org/10.3390/polym10060592

Choi Y, Kim JH, Shin H, Park SD, Yang H (2024) Enhanced interfacial interaction of graphene nanoplatelets/cellulose nanofiber matrix driven by pyranine-based dispersant for efficient thermal managing materials. Compos Sci Technol 255:110698. https://doi.org/10.1016/j.compscitech.2024.110698

Chung DDL, Ozturk M (2022) Electromagnetic skin depth of cement paste and its thickness dependence. J Build Eng 52:104393. https://doi.org/10.1016/j.jobe.2022.104393

Dai Y, Sun N, Jiang D, Wang Z, Ding Q, Zhang Z, Liu Y (2024) Ultrathin and highly flexible layered silver nanowires/carboxymethyl cellulose nanofiber nanocomposite films for electromagnetic interference shielding. Int J Biol Macromol 278:134770. https://doi.org/10.1016/j.ijbiomac.2024.134770

Damnalı OF, Eskizeybek V (2019) Synergistic impact of graphene and carbon nanotubes on waste paper for hybrid nanocomposite substrates. Cellulose 26:3935–3954. https://doi.org/10.1007/s10570-019-02339-7

Ebrahimi A, Dahrazma B, Adelifard M (2020) Facile and novel ambient pressure drying approach to synthesis and physical characterization of cellulose-based aerogels. J Porous Mater 27:1219–1232. https://doi.org/10.1007/s10934-020-00901-4

Françon H et al (2020) Ambient-dried, 3D-printable and electrically conducting cellulose nanofiber aerogels by inclusion of functional polymers. Adv Funct Mater. https://doi.org/10.1002/adfm.201909383

French AD (2014) Idealized powder diffraction patterns for cellulose polymorphs. Cellulose 21:885–896. https://doi.org/10.1007/s10570-013-0030-4

French AD (2017) Glucose, not cellobiose, is the repeating unit of cellulose and why that is important. Cellulose 24:4605–4609. https://doi.org/10.1007/s10570-017-1450-3

Fu C, Sheng Z, Zhang X (2022) Laminated structural engineering strategy toward carbon nanotube-based aerogel films. ACS Nano 16:9378–9388. https://doi.org/10.1021/acsnano.2c02193

Gebrekrstos A, Orasugh JT, Muzata TS, Ray SS (2022) Cellulose-Based sustainable composites: a review of systems for applications in EMI shielding and sensors. Macromol Mater Eng. https://doi.org/10.1002/mame.202200185

Ghazitabar A, Naderi M, Fatmehsari Haghshenas D, Alijani Ashna D (2020) Graphene aerogel/cellulose fibers/magnetite nanoparticles (GCM) composite as an effective Au adsorbent from cyanide solution with favorable electrochemical property. J Mol Liq. https://doi.org/10.1016/j.molliq.2020.113792

Guo T, Li C, Wang Y, Wang Y, Yue J, Tang X-Z (2020a) A highly flexible and porous graphene-based hybrid film with superior mechanical strength for effective electromagnetic interference shielding. Appl Phys A. https://doi.org/10.1007/s00339-020-03965-w

Guo Z, Ren P, Fu B, Ren F, Jin Y, Sun Z (2020b) Multi-layered graphene-Fe_3O_4/poly (vinylidene fluoride) hybrid composite films for high-efficient electromagnetic shielding. Polym Test. https://doi.org/10.1016/j.polymertesting.2020.106652

Guo Z, Ren P, Wang J, Hou X, Tang J, Liu Z, Chen Z, Jin Y, Ren F (2023a) Methylene blue adsorption derived thermal insulating N, S-co-doped TiC/carbon hybrid aerogel for high-efficient absorption-dominant electromagnetic interference shielding. Chem Eng J 451:138667. https://doi.org/10.1016/j.cej.2022.138667

Guo Z, Ren P, Yang F, Wu T, Zhang L, Chen Z, Huang S, Ren F (2023b) MOF-derived Co/C and MXene co-decorated cellulose-derived hybrid carbon aerogel with a multi-interface architecture toward absorption-dominated ultra-efficient electromagnetic interference shielding. ACS Appl Mater Interfaces 15:7308–7318. https://doi.org/10.1021/acsami.2c22447

Han L, Song Q, Li K, Yin X, Sun J, Li H, Zhang F, Ren X, Wang X (2021) Hierarchical, seamless, edge-rich nanocarbon hybrid foams for highly efficient electromagnetic-interference shielding. J Mater Sci Technol 72:154–161. https://doi.org/10.1016/j.jmst.2020.07.020

Haspulat Taymaz B (2023) A novel Ppy/ZnO@Co ternary nanocomposite with enhanced visible light-driven photocatalytic performance. J Taiwan Inst Chem Eng. https://doi.org/10.1016/j.jtice.2023.104741

He X, Xu X, Bo G, Yan Y (2020) Studies on the effects of different multiwalled carbon nanotube functionalization techniques on the properties of bio-based hybrid non-isocyanate polyurethane. RSC Adv 10:2180–2190. https://doi.org/10.1039/c9ra08695a

Hou Z, Zhao C, Cheng J, Chen Z, Wei J, Li H, Xiang D, Wu Y (2024) Preparation and properties of fiber-reinforced polybenzoxazine composite aerogels based on freeze drying and ambient pressure drying methods. Coll Surf a: Physicochem Eng Asp. https://doi.org/10.1016/j.colsurfa.2024.133510

Hu X, Zhang S, Yang B, Hao M, Chen Z, Liu Y, Wang X, Yao J (2023) Preparation of ambient-dried multifunctional cellulose aerogel by freeze-linking technique. Chem Eng J. https://doi.org/10.1016/j.cej.2023.147044

Huang K, Maltais A, Liu J, Wang Y (2022a) Wood cellulose films regenerated from NaOH/urea aqueous solution and treated by hot pressing for food packaging application. Food Biosci 50:102177. https://doi.org/10.1016/j.fbio.2022.102177

Huang Z, Zhang H, Guo M, Zhao M, Liu Y, Zhang D, Terrones M, Wang Y (2022b) Large-scale preparation of electrically conducting cellulose nanofiber/carbon nanotube aerogels: ambient-dried, recyclable, and

3D-printable. Carbon 194:23–33. https://doi.org/10.1016/j.carbon.2022.03.056

Jimenez-Saelices C, Seantier B, Cathala B, Grohens Y (2017) Spray freeze-dried nanofibrillated cellulose aerogels with thermal superinsulating properties. Carbohydr Polym 157:105–113. https://doi.org/10.1016/j.carbpol.2016.09.068

Jyothibasu JP, Kuo D-W, Lee R-H (2019) Flexible and free-standing electrodes based on polypyrrole/carbon nanotube/cellulose composites for supercapacitor application. Cellulose 26:4495–4513. https://doi.org/10.1007/s10570-019-02376-2

Kruzelak J, Kvasnicakova A, Hlozekova K, Hudec I (2021) Progress in polymers and polymer composites used as efficient materials for EMI shielding. Nanoscale Adv 3:123–172. https://doi.org/10.1039/d0na00760a

Langan P, Nishiyama Y, Chanzy H (2001) X-ray structure of mercerized cellulose II at 1 Å resolution. Biomacromol 2:410–416. https://doi.org/10.1021/bm005612q

Lee J, Kim J (2022) Improvement of thermal conductivity and latent heat of cellulose film using surfactant and surface-treated CNT with stearic acid. Compos Part a: Appl Sci Manuf. https://doi.org/10.1016/j.compositesa.2022.106897

Lee JH, Kim YS, Ru HJ, Lee SY, Park SJ (2022) Highly Flexible fabrics/epoxy composites with hybrid carbon nanofillers for absorption-dominated electromagnetic interference shielding. Nanomicro Lett 14:188. https://doi.org/10.1007/s40820-022-00926-1

Li Z, Wang Z, Lu W, Hou B (2018) Theoretical study of electromagnetic interference shielding of 2D MXenes films. Metals 8:652. https://doi.org/10.3390/met8080652

Li M, Zhao Y, Zhang M, Jiang S, Farooq A, Liu L, Ge A, Liu L (2022a) Recent progress in the application of cellulose in electromagnetic interference shielding materials. Macromol Mater Eng. https://doi.org/10.1002/mame.202100899

Li Y, Shi Q, Peng L, Chang M, Zhou F, Gong C, Wu Y, Zhang L (2022b) Carbon nanotubes/cellulose composite aerogels with controllable microstructure for electromagnetic interference shielding. J Appl Polym Sci. https://doi.org/10.1002/app.53535

Li Y, Zhang D, Zhou B, He C, Wang B, Feng Y, Liu C (2022) Synergistically enhancing electromagnetic interference shielding performance and thermal conductivity of polyvinylidene fluoride-based lamellar film with MXene and graphene. Compos Part a: Appl Sci Manuf. https://doi.org/10.1016/j.compositesa.2022.106945

Liang C, Qiu H, Han Y, Gu H, Song P, Wang L, Kong J, Cao D, Gu J (2019) Superior electromagnetic interference shielding 3D graphene nanoplatelets/reduced graphene oxide foam/epoxy nanocomposites with high thermal conductivity. J Mater Chem C 7:2725–2733. https://doi.org/10.1039/c8tc05955a

Liebner F, Potthast A, Rosenau T, Haimer E, Wendland M (2008) Cellulose aerogels: highly porous, ultra-lightweight materials. Holzforschung 62:129–135. https://doi.org/10.1515/HF.2008.051

Liu X, Zhang T, Pang K, Duan Y, Zhang J (2016) Graphene oxide/cellulose composite films with enhanced UV-shielding and mechanical properties prepared in NaOH/urea aqueous solution. RSC Adv 6:73358–73364. https://doi.org/10.1039/c6ra16535d

Liu Y, Liu L, Li Z, Zhao Y, Yao J (2019) Green and facile fabrication of smart cellulose composites assembled by graphene nanoplates for dual sensing. Cellulose 26:9255–9268. https://doi.org/10.1007/s10570-019-02735-z

Liu Z, Khurshid K, Saldaña MDA (2024) Hydrogels and aerogels of cellulose nanofiber derived from barley straw with addition of chitosan using high-intensity ultrasound and supercritical CO_2 drying. Ind Crops Prod. https://doi.org/10.1016/j.indcrop.2024.118755

Long LY, Li FF, Weng YX, Wang YZ (2019) Effects of sodium montmorillonite on the preparation and properties of cellulose aerogels. Polymers (Basel). https://doi.org/10.3390/polym11030415

Ma J, Pu H, He P, Zhao Q, Pan S, Wang Y, Wang C (2021) Robust cellulose-carbon nanotube conductive fibers for electrical heating and humidity sensing. Cellulose 28:7877–7891. https://doi.org/10.1007/s10570-021-04026-y

Ma M, Tao W, Liao X, Chen S, Shi Y, He H, Wang X (2023) Cellulose nanofiber/MXene/FeCo composites with gradient structure for highly absorbed electromagnetic interference shielding. Chem Eng J. https://doi.org/10.1016/j.cej.2022.139471

Ma Z et al (2024) Lightweight dual-functional segregated nanocomposite foams for integrated infrared stealth and absorption-dominant electromagnetic interference shielding. Nano-Micro Lett 16:223. https://doi.org/10.1007/s40820-024-01450-0

Mai T, Wang P-L, Ma M-G (2024) Promising cellulose-based aerogel composites: preparation methods and advanced applications. Compos Part b: Eng. https://doi.org/10.1016/j.compositesb.2024.111559

Najafabadipoor M, Abbaslou H, Bakhtiari S (2025) Structural, morphological, and thermal properties of cellulose nanofibers extracted from waste paper. Chem Papers 79:519–532. https://doi.org/10.1007/s11696-024-03799-3

Nishiyama Y, Langan P, Chanzy H (2002) Crystal structure and hydrogen-bonding system in cellulose i from synchrotron X-ray and neutron fiber diffraction. J Am Chem Soc 124:9074–9082

Nomura S, Kugo Y, Erata T (2020) 13C NMR and XRD studies on the enhancement of cellulose II crystallinity with low concentration NaOH post-treatments. Cellulose 27:3553–3563. https://doi.org/10.1007/s10570-020-03036-6

Oliveira FM, Azadmanjiri J, Wang X, Yu M, Sofer Z (2023) Structure design and processing strategies of MXene-based materials for electromagnetic interference shielding. Small Methods 7:e2300112. https://doi.org/10.1002/smtd.202300112

Pandit N et al (2023) Electrochemical behavior of GNP/CNT porous composite for supercapacitor. Chem Phys Lett. https://doi.org/10.1016/j.cplett.2023.140695

Park J, Kwac LK, Kim HG, Shin HK (2021) Fabrication and characterization of waste wood cellulose fiber/graphene nanoplatelet carbon papers for application as electromagnetic interference shielding materials. Nanomaterials (Basel). https://doi.org/10.3390/nano11112878

Potthast A (2015) Changes in the structure of cellulose aerogels with depolymerization. J Korean Phys Soc 67:742–745. https://doi.org/10.3938/jkps.67.742

Prasad C, Jeong SG, Won JS, Ramanjaneyulu S, Sangaraju S, Kerru N, Choi HY (2024) Review on recent advances in cellulose nanofibril based hybrid aerogels: synthesis, properties and their applications. Int J Biol Macromol 261:129460. https://doi.org/10.1016/j.ijbiomac.2024.129460

Qi H, Liu J, Gaoa S, Mäder E (2013) Multifunctional films composed of carbon nanotubes and cellulose regenerated from alkaline–urea solution. J Mater Chem A 1:2161–2168

Rashad M, Pan F, Asif M, Chen X (2017) Corrosion behavior of magnesium-graphene composites in sodium chloride solutions. J Magnes Alloy 5:271–276. https://doi.org/10.1016/j.jma.2017.06.003

Rodríguez-Fabià S, Torstensen J, Johansson L, Syverud K (2022) Hydrophobisation of lignocellulosic materials part I: physical modification. Cellulose 29:5375–5393. https://doi.org/10.1007/s10570-022-04620-8

Rosenaua T, Potthast A, Sixta H, Kosma P (2001) The chemistry of side reactions and byproduct formation in the system NMMO/cellulose (Lyocell process). Prog Polym Sci 26:1763–1837

Saini P, Choudhary V, Singh BP, Mathur RB, Dhawan SK (2009) Polyaniline–MWCNT nanocomposites for microwave absorption and EMI shielding. Mater Chem Phys 113:919–926. https://doi.org/10.1016/j.matchemphys.2008.08.065

Salem KS et al (2023) Comparison and assessment of methods for cellulose crystallinity determination. Chem Soc Rev 52:6417–6446. https://doi.org/10.1039/d2cs00569g

Sankhla S, Neogi S (2024) Ambient-dried, scalable and biodegradable cellulose nanofibers aerogel for oil-spill cleanup. J Environ Chem Eng. https://doi.org/10.1016/j.jece.2024.112745

Scherrer P (1918) Bestimmung der Größe und der inneren Struktur von Kolloidteilchen mittels Röntgenstrahlen. Nachrichten Von der Gesellschaft der Wissenschaften Zu Göttingen, Mathematisch-Physikalische Klasse 1918:98–100

Schiele C, Di A, Hadi SE, Rangaiah PKB, Augustine R, Bergström L (2024) Hybrid foams based on multi-walled carbon nanotubes and cellulose nanocrystals for anisotropic electromagnetic shielding and heat transport. Adv Mater Interfaces. https://doi.org/10.1002/admi.202300996

Segal L, Creely JJ, Martin AE, Conrad CM (1959) An empirical method for estimating the degree of crystallinity of native cellulose using the x-ray diffractometer. Textile Res J 29:786–794. https://doi.org/10.1177/004051755902901O

Song P et al (2021) Lightweight, flexible cellulose-derived carbon aerogel@reduced graphene oxide/PDMS composites with outstanding EMI shielding performances and excellent thermal conductivities. Nanomicro Lett 13:91. https://doi.org/10.1007/s40820-021-00624-4

Srasri K, Thongroj M, Chaijiraaree P, Thiangtham S, Manuspiya H, Pisitsak P, Ummartyotin S (2018) Recovery potential of cellulose fiber from newspaper waste: an approach on magnetic cellulose aerogel for dye adsorption material. Int J Biol Macromol 119:662–668. https://doi.org/10.1016/j.ijbiomac.2018.07.123

Tan YQ, Luo H, Zhou XS, Peng SM, Zhang HB (2018) Boron carbide composites with highly aligned graphene nanoplatelets: light-weight and efficient electromagnetic interference shielding materials at high temperatures. RSC Adv 8:39314–39320. https://doi.org/10.1039/c8ra07351a

Tchessalov S, Shalaev E, Bhatnagar B, Nail S, Alexeenko A, Jameel F, Srinivasan J, Dekner M, Sahni E, Schneid S, Kazarin P (2022) Best practices and guidelines (2022) for scale-up and tech transfer in freeze-drying based on case studies part 1: challenges during scale up and transfer. AAPS PharmSciTech 24:11. https://doi.org/10.1208/s12249-022-02463-x

Vendange V, Flavin E (1996) Gyromagnetic microwave resonance of cobalt-aluminoborosilicate nanocomposites. J Mater Sci Lett 15:137–141

Wang Q, Wang Y, Meng Q, Wang T, Guo W, Wu G, You L (2017) Preparation of high antistatic HDPE/polyaniline encapsulated graphene nanoplatelet composites by solution blending. RSC Adv 7:2796–2803. https://doi.org/10.1039/c6ra26458a

Wang L, Ma Z, Zhang Y, Chen L, Cao D, Gu J (2021) Polymer-based EMI shielding composites with 3D conductive networks: a mini-review. SusMat 1:413–431. https://doi.org/10.1002/sus2.21

Wang M-L, Zhou Z-H, Zhu J-L, Lin H, Dai K, Huang H-D, Li Z-M (2022) Tunable high-performance electromagnetic interference shielding of intrinsic N-doped chitin-based carbon aerogel. Carbon 198:142–150. https://doi.org/10.1016/j.carbon.2022.07.016

Wang L, Shen H, Zhang H, Xu D, Zhou J (2024a) Fabrication of anisotropic carbon aerogels from cellulose nanofiber/graphene oxide composites for electromagnetic interference shielding. J Alloys Compd. https://doi.org/10.1016/j.jallcom.2024.173505

Wang Y, Qi J, Zhang M, Xu T, Zheng C, Yuan Z, Si C (2024b) Cellulose-based aerogels, films, and fibers for advanced biomedical applications. Chem Eng J. https://doi.org/10.1016/j.cej.2024.154434

Wernersson E, Stenqvist B, Lund M (2015) The mechanism of cellulose solubilization by urea studied by molecular simulation. Cellulose 22:991–1001. https://doi.org/10.1007/s10570-015-0548-8

Wu C, Zeng L, Chang G, Zhou Y, Yan K, Xie L, Xue B, Zheng Q (2023a) Composite phase change materials embedded into cellulose/polyacrylamide/graphene nanosheets/silver nanowire hybrid aerogels simultaneously with effective thermal management and anisotropic electromagnetic interference shielding. Adv Compos Hybrid Mater. https://doi.org/10.1007/s42114-022-00618-9

Wu N et al (2023b) Ultrathin cellulose nanofiber assisted ambient-pressure-dried, ultralight, mechanically robust. Multifunctional MXene Aerogels Adv Mater 35:e2207969. https://doi.org/10.1002/adma.202207969

Wulandari WT, Rochliadi A, Arcana IM (2016) Nanocellulose prepared by acid hydrolysis of isolated cellulose from sugarcane bagasse. IOP Conf Ser: Mater Sci Eng. https://doi.org/10.1088/1757-899x/107/1/012045

Xiong B, Zhao P, Hu K, Zhang L, Cheng G (2014) Dissolution of cellulose in aqueous NaOH/urea solution: role of urea. Cellulose 21:1183–1192. https://doi.org/10.1007/s10570-014-0221-7

Xu F, Kim Y-l, Oh S-Y, Cho B-U (2023) Facile synthesis of porous cellulose aerogel beads with tunable core–shell microstructures and physical properties. J Ind Eng Chem 126:160–170. https://doi.org/10.1016/j.jiec.2023.06.006

Yang JC, Wang XJ, Zhang G, Wei ZM, Long SR, Yang J (2020) Segregated poly(arylene sulfide sulfone)/graphene nanoplatelet composites for electromagnetic interference shielding prepared by the partial dissolution method. RSC Adv 10:20817–20826. https://doi.org/10.1039/d0ra02705g

Yang G, Kong H, Chen Y, Liu B, Zhu D, Guo L, Wei G (2022) Recent advances in the hybridization of cellulose and carbon nanomaterials: interactions, structural design, functional tailoring, and applications. Carbohydr Polym 279:118947. https://doi.org/10.1016/j.carbpol.2021.118947

Yang J, Wang H, Zhang Y, Zhang H, Gu J (2024) Layered structural PBAT composite foams for efficient electromagnetic interference shielding. Nano-Micro Lett 16:31. https://doi.org/10.1007/s40820-023-01246-8

Yang J, Wang H, Zhang H, Lin P, Gao H, Xia Y, Liao X (2025) Multistage microcellular waterborne polyurethane composite with optionally low-reflection behavior for ultra-efficient electromagnetic interference shielding. J Mater Sci Technol 208:132–140. https://doi.org/10.1016/j.jmst.2024.04.061

Yıldırım F (2023) Effect Low-Velocity impact damage on the electromagnetic interference shielding effectiveness of CFRP composites Konya Journal of. Eng Sci 11:958–972

Yue X, Zhang T, Yang D, Qiu F, Li Z (2018) Hybrid aerogels derived from banana peel and waste paper for efficient oil absorption and emulsion separation. J Clean Prod 199:411–419. https://doi.org/10.1016/j.jclepro.2018.07.181

Yun J, Lee J, Kim J, Lee J, Choi W (2024) Hexagonal boron nitride nanosheets/graphene nanoplatelets/cellulose nanofibers-based multifunctional thermal interface materials enabling electromagnetic interference shielding and electrical insulation. Carbon. https://doi.org/10.1016/j.carbon.2024.119397

Zhang T, Zhang W, Xi H, Li Q, Shen M, Ying G, Zhang J (2021) Polydopamine functionalized cellulose-MXene composite aerogel with superior adsorption of methylene blue. Cellulose 28:4281–4293. https://doi.org/10.1007/s10570-021-03737-6

Zhang M, Su M, Qin Y, Liu C, Shen C, Ma J, Liu X (2023) Photothermal ultra-high molecular weight polyethylene/MXene aerogel for crude oil adsorption and water evaporation. 2D Materials. https://doi.org/10.1088/2053-1583/acc3aa

Zhang D, Du K, Shi P, Wu X, Zhang S (2024a) Carboxyl functionalized cellulose nanofibril for polyvinyl alcohol based aerogels with enhanced pore structures and mechanical properties. Ind Crop Prod. https://doi.org/10.1016/j.indcrop.2024.118294

Zhang L-Q et al (2024b) Multifunctional cellulose composite films with dual-continuous CNT/BN networks for synchronously enhanced electromagnetic interference shielding ability and thermal conductivity. Cellulose 31:2397–2412. https://doi.org/10.1007/s10570-024-05767-2

Zhang T, Wu C, Ji B, Li B, Du X (2024c) Flexible regenerated cellulose composite films with sandwich structures for high-performance electromagnetic interference shielding. J Mater Sci 59:5634–5646. https://doi.org/10.1007/s10853-024-09543-2

Zhang Y, Min P, Yue G, Niu B, Li L, Yu ZZ, Zhang HB (2024d) Emulsion-Based multiscale structural design realizes lightweight and superelastic graphene aerogels for electromagnetic interference shielding. Small 20:2405950. https://doi.org/10.1002/smll.202405950

Zhang Y, Zou X, Zhang S, Ma Z, Zhang G (2024e) Flexible multifunctional magnetic-conductive Janus nanocomposite films towards highly-efficient electromagnetic interference shielding and thermal management. Compos Sci Technol 256:110756. https://doi.org/10.1016/j.compscitech.2024.110756

Zhao H, Gao T, Yun J, Chen L (2024) Robust liquid metal reinforced cellulose nanofiber/MXene composite film with Janus structure for electromagnetic interference shielding and electro-/photothermal conversion applications. J Mater Sci Technol 191:23–32. https://doi.org/10.1016/j.jmst.2023.12.035

Zheng H, Zhou J, Du Y, Zhang L (2002) Cellulose/chitin films blended in NaOH/urea aqueous solution. J Appl Polym Sci 86:1679–1683. https://doi.org/10.1002/app.11043

Zheng W, Xie H, Li J, Yu H, Tang Z, Tian G, Wang Q, Wang T (2024) Design of polyimide/carbon nanotube@Ag@polyimide/graphene composite aerogel for infrared stealth and electromagnetic interference protection. Compos Part a: Appl Sci Manuf. https://doi.org/10.1016/j.compositesa.2024.108371

Zhou T, Cheng X, Pan Y, Li C, Gong L (2018) Mechanical performance and thermal stability of polyvinyl alcohol–cellulose aerogels by freeze drying. Cellulose 26:1747–1755. https://doi.org/10.1007/s10570-018-2179-3

Zhou S, Apostolopoulou-Kalkavoura V, Tavares da Costa MV, Bergstrom L, Stromme M, Xu C (2019) Elastic aerogels of cellulose nanofibers@metal-organic frameworks for thermal insulation and fire retardancy. Nanomicro Lett 12:9. https://doi.org/10.1007/s40820-019-0343-4

Zhou Y, Yao J, Chen Q, Xiao J, Zhang N, Zhuang Y, Yang H (2024) Study on the preparation of recycled boards instead of wood boards from waste cellulose. Materialwiss Werkstofftech 55:375–383. https://doi.org/10.1002/mawe.202300117

Zhu G, Giraldo Isaza L, Huang B, Dufresne A (2022) Multifunctional nanocellulose/carbon nanotube composite aerogels for high-efficiency electromagnetic interference shielding. ACS Sustain Chem Eng 10:2397–2408. https://doi.org/10.1021/acssuschemeng.1c07148

Zong Z, Ren P, Guo Z, Wang J, Chen Z, Jin Y, Ren F (2022a) Three-dimensional macroporous hybrid carbon aerogel with heterogeneous structure derived from MXene/cellulose aerogel for absorption-dominant electromagnetic interference shielding and excellent thermal insulation performance. J Coll Interface Sci 619:96–105. https://doi.org/10.1016/j.jcis.2022.03.136

Zong Z, Ren P, Guo Z, Wang J, Hu J, Chen Z, Jin Y, Wang F, Ren F (2022b) Synergistic effect of 2D TiC and 1D CNT towards absorption-dominant high-performance electromagnetic interference shielding in 3D macroporous carbon aerogel. Carbon 197:40–51. https://doi.org/10.1016/j.carbon.2022.06.022